

The measured  $l_{pl}$  is 0.6 mm (Fig. 4 legend), implying that the constant  $\Lambda = 0.7$ .

Time-lapse video is used to measure the average erosion rate of the dense layer by flow into established conduits. The time-derivative of the position of the density interface indicates an average erosion rate of 3–5 mm h<sup>-1</sup>. From equations (3) and (5), the erosion rate is

$$q_{pl} = V_{pl} \frac{l_{pl}^2}{L^2} = \frac{\Lambda^2 \kappa Ra^{1/3}}{H \lambda_d B} \quad (6)$$

which is consistent with refs 9 and 16, and which predicts  $q_{pl} = 5 \text{ mm h}^{-1}$  (Fig. 3).

Applying our results to the Earth requires constraints on  $Ra$ ,  $B$ ,  $\lambda_d$  and  $\lambda_h$ .  $Ra$  for mantle convection driven by core cooling is in the range  $10^7$ – $10^8$ . The data in Fig. 3 imply that  $\lambda_d$  needs to be in excess of  $10^1$ – $10^2$  in order for fixed plumes to occur. In addition, we take  $\lambda_h = 10^2$  (ref. 24) and  $B = 0.5$ , along with typical values of  $\kappa = 10^{-6} \text{ m}^2 \text{ s}^{-1}$  and  $H = 3 \times 10^6 \text{ m}$ . Assuming that mantle starting plumes are dynamically similar to thermals, equations (2) and (4) imply that tendrils entrained by flow into starting plumes are less than 1 km in radius, and that the associated erosion rates are of the order of  $10^{-8}$ – $10^{-7} \text{ km Myr}^{-1}$ . On the other hand, because  $V_{pl} \gg V_{th}$ , equations (5) and (6) predict that tendrils entrained into established low-viscosity conduits are 5–10 km in radius, and the resultant entrainment rate is expected to be of the order of  $10^{-2}$ – $10^{-3} \text{ km Myr}^{-1}$ . If a typical dense layer is, say, 100–300 km high, these erosion rates imply that the layer could persist for times comparable to, or longer than, the age of the Earth. Finally, equation (3) predicts that, in the presence of a dense layer, the spacing between mantle plumes is of the order of  $10^3 \text{ km}$ . This value is compatible with the distribution of hotspots in the Pacific, which appear to overlie the ultra-low-velocity zone<sup>3</sup>, when their positions are extrapolated to the core–mantle boundary<sup>3,25,30</sup>.

We have shown that a dense, low-viscosity compositional boundary layer at the base of the mantle may determine the location, relative fixity and spacing of mantle plumes. Moreover, we have argued that entrainment from this low-viscosity layer may influence the composition of plumes and be important in establishing long-lived, low-viscosity conduits extending from the thermal boundary layer at the base of the mantle to the base of the lithosphere. Our results may resolve a basic conundrum in mantle dynamics—that hotspots remain approximately fixed in space relative to each other for timescales much longer than the time required for a plume to rise through the mantle. □

Received 26 October 2001; accepted 15 July 2002; doi:10.1038/nature00979.

1. Lay, T., Williams, Q. & Garnero, E. J. The core–mantle boundary layer and deep Earth dynamics. *Nature* **392**, 461–468 (1998).
2. Wyssession, M. E. Large-scale structure at the core–mantle boundary from diffracted waves. *Nature* **382**, 244–248 (1996).
3. Castle, J. C., Creager, K. C., Winchester, J. P. & van der Hilst, R. D. Shear wave speeds at the base of the mantle. *J. Geophys. Res.* **105**, 21543–21557 (2000).
4. Gurnis, M., Wyssession, M. E., Knittle, E. & Buffett, B. A. (eds) *The Core–Mantle Region Monograph 28* (American Geophysical Union, Washington DC, 1998).
5. Garnero, E. J. Heterogeneity of the lowermost mantle. *Annu. Rev. Earth Planet. Sci.* **28**, 509–537 (2000).
6. Knittle, E. & Jeanloz, R. The Earth's core–mantle boundary: Results of experiments at high pressures and temperatures. *Science* **251**, 1438–1453 (1991).
7. Brandon, A. D. et al. Coupled <sup>186</sup>Os and <sup>187</sup>Os evidence for core–mantle interaction. *Science* **280**, 1570–1573 (1998).
8. Williams, Q. & Garnero, E. J. Seismic evidence for partial melt at the base of the Earth's mantle. *Science* **273**, 1528–1530 (1996).
9. Davaille, A. Simultaneous generation of hotspots and superswells by convection in a heterogeneous planetary mantle. *Nature* **402**, 756–760 (1999).
10. Olson, P. & Kincaid, C. Experiments on the interaction of thermal convection and compositional layering at the base of the mantle. *J. Geophys. Res.* **96**, 4347–4354 (1991).
11. Sleep, N. H. Gradual entrainment of a chemical layer at the base of the mantle by overlying convection. *Geophys. J. Int.* **95**, 437–447 (1998).
12. Montague, N. L. & Kellogg, L. H. Numerical models of a dense layer at the base of the mantle and implications for the geodynamics of D'. *J. Geophys. Res.* **105**, 11101–11114 (2000).
13. Farnetani, C. G. Excess temperature of mantle plumes: the role of chemical stratification across D'. *Geophys. Res. Lett.* **24**, 1583–1586 (1997).

14. Tackley, P. J. The strong heterogeneity caused by deep mantle layering. *Geochem. Geophys. Geosyst.* **3**, U1–U22 (2002).
15. van Keken, P. E. et al. A comparison of methods for the modeling of thermochemical convection. *J. Geophys. Res.* **102**, 22477–22495 (1997).
16. Gonnermann, H. M., Manga, M. & Jellinek, A. M. Dynamics and longevity of an initially stratified mantle. *Geophys. Res. Lett.* **29**, 10.1029/2002GL014851 (2002).
17. Neavel, K. E. & Johnson, A. M. Entrainment in compositionally buoyant plumes. *Tectonophysics* **200**, 1–15 (1991).
18. Manga, M. & Weeraratne, D. Experimental study of non-Boussinesq Rayleigh–Benard convection at high Rayleigh and Prandtl numbers. *Phys. Fluids* **11**, 2969–2976 (1999).
19. Sparrow, E. M., Husar, R. B. & Goldstein, R. J. Observations and other characteristics of thermals. *J. Fluid Mech.* **41**, 793–802 (1970).
20. Davaille, A. Two-layer thermal convection in miscible viscous fluids. *J. Fluid Mech.* **379**, 223–253 (1999).
21. Olson, P., Schubert, G. & Anderson, C. Structure of axisymmetric mantle plumes. *J. Geophys. Res.* **98**, 6829–6844 (1993).
22. Turner, J. S. *Buoyancy Effects in Fluids* (Cambridge Univ. Press, Cambridge, 1973).
23. Lister, J. R. & Kerr, R. C. The effect of geometry on the gravitational instability of a buoyant region of viscous fluid. *J. Fluid Mech.* **202**, 577–594 (1989).
24. Nataf, H.-C. Mantle convection, plates, and hotspots. *Tectonophysics* **187**, 361–377 (1991).
25. Sleep, N. H. Time dependence of mantle plumes: Some simple theory. *J. Geophys. Res.* **97**, 20007–20019 (1992).
26. Schaeffer, N. & Manga, M. Interaction of rising and sinking mantle plumes. *Geophys. Res. Lett.* **28**, 455–458 (2001).
27. Neavel, K. E. & Johnson, A. M. Entrainment in compositionally buoyant plumes. *Tectonophysics* **200**, 1–15 (1991).
28. Jellinek, A. M., Lenardic, A. & Manga, M. The influence of interior mantle temperature on the structure of plumes: Heads for Venus, Tails for the Earth. *Geophys. Res. Lett.* **29**, 10.1029/2001GL014624 (2002).
29. Martin, D. & Campbell, I. H. Laboratory modeling of convection in magma chambers: Crystallization against sloping floors. *J. Geophys. Res.* **93**, 7974–7988 (1988).
30. Steinberger, B. & O'Connell, R. J. Advection of plumes in mantle flow: implications for hotspot motion, mantle viscosity and plume distribution. *Geophys. J. Int.* **132**, 412–434 (1998).

**Acknowledgements**

We thank A. Davaille for comments on the previous version of the manuscript, and L. H. Kellogg, R. C. Kerr, M. A. Richards and N. Sleep for comments on earlier versions. This work was supported by the National Science Foundation and The Miller Institute for Basic Research in Science.

**Competing interests statement**

The authors declare that they have no competing financial interests.

Correspondence and requests for materials should be addressed to A.M.J. (e-mail: markj@seismo.berkeley.edu).

.....  
**Seismic evidence for catastrophic slab loss beneath Kamchatka**

**Vadim Levin\***, **Nikolai Shapiro\*†**, **Jeffrey Park\*** & **Michael Ritzwoller\*†**

\* *Department of Geology and Geophysics, Box 208109, Yale University, New Haven, Connecticut 06520, USA*

† *Department of Physics, University of Colorado, Boulder, Colorado 80309, USA*

.....  
**In the northwest Pacific Ocean, a sharp corner in the boundary between the Pacific plate and the North American plate joins a subduction zone running along the southern half of the Kamchatka peninsula<sup>1</sup> with a region of transcurrent motion along the western Aleutian arc<sup>1,2</sup>. Here we present images of the seismic structure beneath the Aleutian–Kamchatka junction and the surrounding region, indicating that: the subducting Pacific lithosphere terminates at the Aleutian–Kamchatka junction; no relic slab underlies the extinct northern Kamchatka volcanic arc; and the upper mantle beneath northern Kamchatka has unusually slow shear wavespeeds. From the tectonic and volcanic evolution of Kamchatka over the past 10 Myr (refs 3–5) we infer that at least two episodes of catastrophic slab loss have occurred. About 5 to 10 Myr ago, catastrophic slab loss shut down island-arc volcanic**

activity north of the Aleutian–Kamchatka junction. A later episode of slab loss, since about 2 Myr ago, seems to be related to the activity of the world’s most productive island-arc volcano, Klyuchevskoy<sup>6</sup>. Removal of lithospheric mantle is commonly discussed in the context of a continental collision, but our findings imply that episodes of slab detachment and loss are also important agents in the evolution of oceanic convergent margins.

At convergent margins the descent of the lithospheric slab into the upper mantle may give way to tearing, detachment, and sinking of the slab material, accompanied by uplift, extension and distinctive magmatism<sup>7–9</sup>. Ongoing slab tears are proposed for the Apennines<sup>8</sup> and Taiwan<sup>9</sup>, and the foundering of lithospheric mantle has been documented beneath Tibet<sup>10</sup> and the Alboran Sea<sup>11</sup>. There is, therefore, growing evidence for lithospheric mantle detachment as a mechanism for the rejuvenation of continental lithosphere. Evidence for similar detachment of the mantle lithosphere in an oceanic margin setting is much weaker. Here, we present tomographic images of the shallow mantle from surface-wave dispersion data that, together with other geophysical and geochemical evidence, imply several episodes of slab removal beneath the Kamchatka peninsula of the Russian Far East. We argue that lithospheric detachment is essential to the evolution of this and other oceanic-margin subduction zones.

Deep subduction-related earthquakes range from 400 km beneath southernmost Kamchatka to ~200 km at the Aleutian–Kamchatka junction (AKJ), and slab dip decreases from 55° to 35° (ref. 12). A chain of volcanoes along the eastern coast of Kamchatka traces the 100-km depth-contour of the subducted Pacific lithosphere, culminating in a cluster of volcanoes inland of the AKJ. The distribution of volcanic rocks on the peninsula suggests geologically recent rearrangement of the associated subduction zones<sup>13</sup>. Before about 10 Myr ago, island-arc magmatism extended north of the AKJ along the mid-Kamchatka volcanic belt (Fig. 1). That volcanism changed character afterwards<sup>13,14</sup> and is now extinct<sup>4</sup>.

The dynamics of the Kamchatka subduction zone reflect the

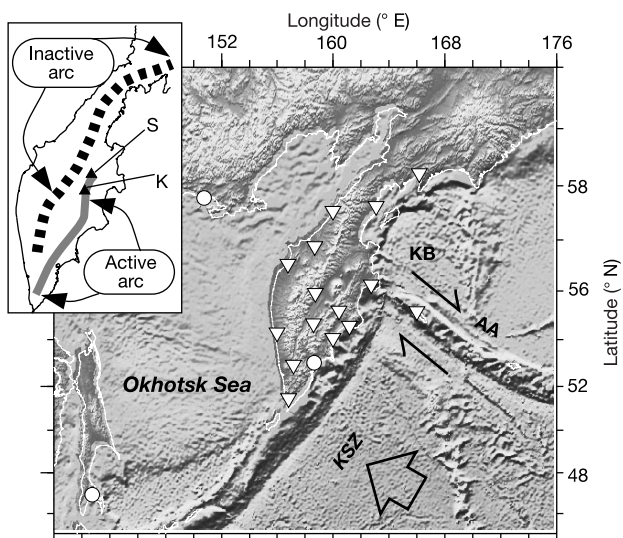


**Figure 1** An overview map of the Aleutian–Kamchatka junction (AKJ), showing the tectonic setting and the observational system used. Shaded topography outlines the mid-Kamchatka (Sredinny) range of Kamchatka that is a locus of past island-arc volcanism. Open symbols denote permanent (circle) and temporary (triangle) seismic observatories. The large open arrow shows the Pacific plate motion direction, filled half-arrows denote a region of distributed strike–slip deformation. Inset, outlines of two volcanic chains of Kamchatka, and locations of the Klyuchevskoy volcanic group (K) and the Sheveluch volcano (S). Geographic and tectonic features marked are the Aleutian Arc (AA), the Kamchatka subduction zone (KSZ) and the Komandorsky basin (KB).

configuration of recently and presently subducted oceanic lithosphere, and the mantle flow regime at the AKJ. The fate of the relict slab beneath northern Kamchatka is unknown, as no deep earthquakes occur north of the AKJ<sup>12</sup>. A relict slab beneath the western Aleutian islands<sup>15</sup> could accommodate the change in plate-boundary type at the AKJ by folding over the corner, but petrologic data<sup>16</sup> suggest a gap in subducted lithosphere between the AKJ and Adak island in the central Aleutians.

Tomographic imaging of the upper-mantle compressional velocity ( $V_p$ ) structure in the AKJ region with body waves<sup>17,18</sup> is limited by a scarcity of stations and seismicity north of the AKJ, and poor crossing-ray coverage from teleseismic events in the uppermost mantle. Surface-wave dispersion tomography is better suited for imaging shear velocity ( $V_s$ ) in the key depth range (50–150 km) for lithospheric detachment. The primary data for our tomographic  $V_s$

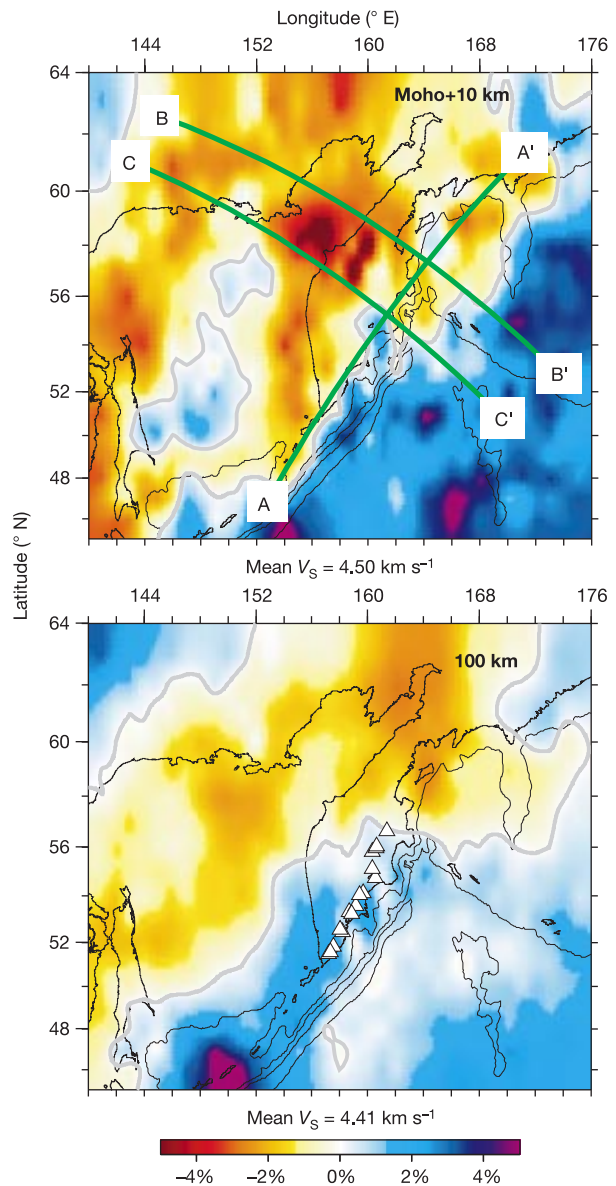


**Figure 2** Maps of seismic velocity distribution. Deviations from the mean regional value are shown for the depth of 100 km (bottom panel) and for 10 km beneath the crust–mantle transition (top panel). Variations in crustal thickness imply an uneven surface in the latter graph. Light grey lines show contours of mean regional velocity. Coastlines and outlines of submarine bathymetry are shown for reference. Top, green lines show tracks of the vertical profiles presented in Fig. 3. Bottom, volcanoes with post-1900 eruptions are plotted as open triangles.

model consists of a large set of dispersion curves for broadband Rayleigh and Love wave group and phase velocities<sup>19,20,21</sup>. Because long propagation paths in global tomographic studies can limit lateral resolution, we added complementary dispersion data (group velocity measurements for 1,432 Rayleigh and 649 Love source–receiver paths) from a year-long deployment of portable seismic stations in Kamchatka<sup>30</sup>. Period-specific dispersion maps were found with “diffraction tomography”<sup>22</sup>, a technique based on a physical model of the surface wave Fresnel zone. These dispersion maps were subjected to nonlinear Monte-Carlo inversion<sup>23</sup> for an ensemble of acceptable  $V_S$  models of the crust and the uppermost mantle on a  $1^\circ \times 1^\circ$  grid across the region of study.

Descending cold mantle lithosphere should be characterized by a positive  $V_S$  anomaly with thin ( $\sim 200$  km) tabular geometry. The joint inversion of short- and intermediate-period group speeds with long-period phase speed data greatly reduces the ensemble variance of the acceptable  $V_S$  models at individual gridpoints, and affords tighter lateral resolution in the shallow mantle. Vertical resolution is improved by constraining crustal structure with body-wave reverberations<sup>24</sup>. The multiplicity of sources and receivers means that lateral resolution for our study region is better than the global

average. Vertical resolution experiments establish that the high- $V_S$  signature of a subducting slab can be estimated reliably to depths of at least 200 km.

Figures 2, 3 and 4a show that a fast  $V_S$  anomaly delineates the descending Pacific plate beneath southern Kamchatka (profile

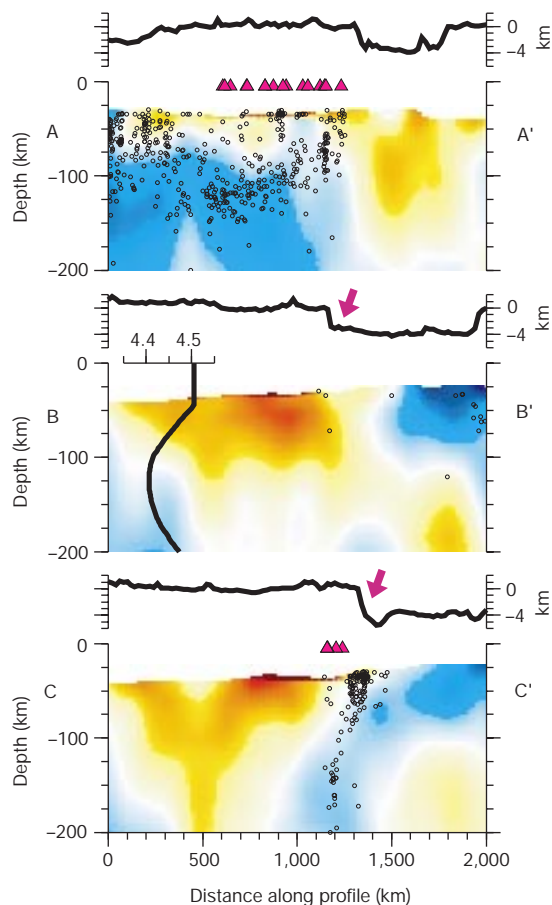


**Figure 3** Vertical cross-sections through the shear velocity model with the same colour scale as in Fig. 2, vertical exaggeration 1:5. Colours indicate anomalies in S-wave velocity relative to the regional one-dimensional distribution shown in profile B–B'. The shallow part of the model is removed to accentuate the details of the deeper structures. Surface topography/bathymetry along profile tracks is plotted (in km) above each profile. Earthquake hypocentres within 20 km of the profile plane are shown by small circles. Volcanoes with post-1900 eruptions within 100 km of the profile are shown by triangles. Trench location is marked by the arrow of profiles B–B' and C–C'. Subducted slab of the Komandorsky basin lithosphere would have been to the left of the arrow on profile B–B'. In the panel showing profile B–B', the inset horizontal axis shows shear wave velocity,  $V_S$ , in  $\text{kms}^{-1}$ .

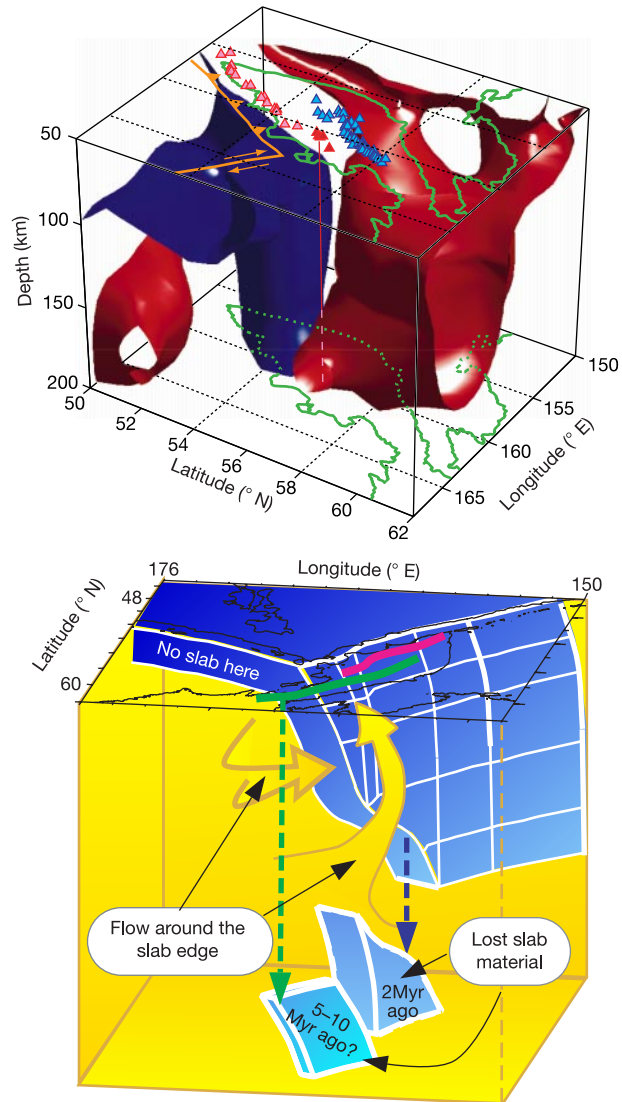


**Figure 4** Structure and geodynamics of the AKJ. **a**, Isosurface representation of the  $V_S$  model beneath the AKJ, in which the model was laterally smoothed with a gaussian filter ( $\sigma = 100$  km) to highlight the dominant large-scale features. The blue surface (+0.8%) represents the high seismic velocity oceanic lithosphere subducting beneath southern Kamchatka. The red surface (–2.2%) reflects low seismic velocity material beneath northern Kamchatka. The coastline (green) and the modern plate boundary (salmon-coloured arrows and line) are identified. Pink and red triangles are locations of active volcanoes where red triangles correspond to the Klyuchevskoy and Sheveluch volcanic groups located above the edge of the subducted slab; blue triangles are the locations of Holocene volcanoes in the presently inactive mid-Kamchatka volcanic belt; the red line (solid and dashed) shows the position of the volcanic group marked by red triangles relative to the structure at depth. In the late Miocene and into the Pliocene, volcanic activity in this belt extended up to  $60^\circ$  N (ref. 13). **b**, A depiction of the subducting Pacific plate (blue). Outlines of the active (magenta) and inactive (green) volcanic arcs are shown. Fragments of the younger Komandorsky lithosphere (lighter blue) and the older Pacific lithosphere (deeper blue) has detached from the lithospheric mantle beneath the AKJ (as shown by dashed arrows), at 5–10 and 2 Myr ago, respectively. This allowed warmer asthenospheric material (yellow arrows) to flow both around the subducting slab and upwards towards the surface.

C–C'), weakens northward, and terminates beneath the AKJ (profile A–A'). The anomaly is particularly weak where seismicity gets shallower beneath the AKJ. A slow anomaly beneath the Okhotsk Sea is contiguous with a deeper slow anomaly under the Komandorsky basin (profile B–B').

These  $V_S$  images, historical seismicity<sup>12</sup>, and earlier  $V_P$  tomography<sup>17,18</sup> provide evidence that the current oceanic lithosphere of the Pacific plate terminates at the AKJ. Neither the  $V_S$  nor the previous  $V_P$  tomographic images detect relict slab material beneath northern Kamchatka from the approximately 10 Myr ago subduction of the Komandorsky basin<sup>4</sup>. The results from  $V_S$  tomography, in combination with other geophysical and geological evidence, show that the upper mantle beneath northern Kamchatka has undergone major changes since 10 Myr ago and that subduction dynamics beneath Kamchatka is far from steady-state. We argue that this instability in the upper mantle involves at least two episodes of slab loss (Fig. 4b). Specifically, we propose that in the first episode, which occurred between 5 Myr and 10 Myr ago, a relict slab created by westward subduction of the Komandorsky basin lithosphere detached. In the second episode, since 2 Myr ago, a fragment of the present Pacific plate detached and sank into the mantle.

We associate the first episode of slab loss, that is, detachment of Komandorsky lithosphere, with the latest (Pliocene-epoch to the Quaternary period) stage of the volcanism in northern Kamchatka. The absence of an aseismic slab combined with a progressive change from island-arc volcanism to rift-like volcanism at about 5 Myr ago<sup>13,14</sup> suggest thermal rejuvenation of the mantle lithosphere beneath northern Kamchatka since that time. Alkalic volcanism consistent with low partial-fraction pressure–release melting is a likely consequence of asthenospheric upwelling<sup>3,13,14</sup>. Petrologic evidence for a “slab melt” component in volcanic rocks from the now-extinct northern Kamchatka arc<sup>25</sup> may be associated with the remelting of dacite-veined peridotite within the supra-slab mantle wedge, a lithology reported in northern Kamchatka mantle xenoliths<sup>26</sup>. Low values of  $V_S$  imaged in the asthenosphere beneath northern Kamchatka further support the idea of the influx of warm asthenospheric material towards the surface.

The second episode of slab detachment, involving the loss of an edge fragment of the Pacific plate within the past 2 Myr ago or so, is inferred on the basis of Pliocene–Pleistocene tectonic motions, as well as the volcanism near the AKJ<sup>5</sup>. The presently subaerial central Kamchatka depression near the AKJ lay beneath sea level in the Pliocene epoch<sup>3</sup>. Active volcanism in the Klyuchevskoy volcanic cluster lies above the slab edge itself (Fig. 4a), and dates back only about 50 kyr ago<sup>27</sup>. The current output of Klyuchevskoy volcano exceeds that of any other island-arc volcano<sup>6</sup>. Its lavas are characterized by high temperatures of equilibration<sup>28</sup>, consistent with pressure–release melting induced by a transient lofting of the slab edge<sup>5,6</sup>. Slab-edge lofting causes the inland shift of the island-arc volcanism at the AKJ relative to the volcanic arc further south<sup>12</sup>. A pulse of subduction-derived volatiles is an alternative cause of intensified volcanism, but contradicts geochemical evidence for modest sediment input<sup>23</sup> and long mantle-wedge residence times of volatiles<sup>29</sup>. In addition, the northern part of the fast  $V_S$  anomaly that we associate with the Pacific lithosphere is very weak (~1%), and its border is highly irregular. This weakening probably reflects the loss of material from the side edge of the subducting slab, through dynamic or gravitational instability<sup>7</sup> or through erosion by mantle flow around the corner of the subduction zone<sup>3</sup>. Such flow would have been obstructed if the Komandorsky lithosphere had not detached. Further evidence for such flow, together with some material ascent towards the surface beneath northwestern Kamchatka, comes from seismic anisotropy<sup>5,30</sup>, and from an exceptionally slow  $V_S$  anomaly to the northwest of the AKJ that is apparently connected to a deeper body of slow material beneath the Komandorsky basin (Fig. 4a). This flow regime may be responsible for a ‘slab melt’, or adakite, petrologic signature at Sheveluch, the north-

ernmost active volcano in Kamchatka, through partial melting of the slab edge<sup>16</sup>. It is likely that the erosion of the slab edge is an continuing process.

Our findings emphasize the importance of slab detachment and loss as an agent in the evolution of convergent margins. They also illustrate the complexity of dynamical, petrological and tectonic processes that occur near slab edges. □

Received 19 March; accepted 8 July 2002; doi:10.1038/nature00973.

- Zonenshain, L. P., Kuzmin, M. I. & Natapov, L. M. *Geology of the USSR: A Plate-Tectonic Synthesis* (AGU, Geodynamics Series No. 21, American Geophysical Union, Washington DC, 1990).
- Geist, E. L. & Scholl, D. W. Application of continuum models to deformation of the Aleutian island arc. *J. Geophys. Res.* **97**, 4953–4967 (1992).
- Erlich, E. N. & Gorshkov, G. S. (eds) Quaternary volcanism and tectonics in Kamchatka. *Bull. Volcanol.* **42**, 1–298 (1979).
- Honthaas, C., Bellon, H., Kepezhinskas, P. K. & Maury, R. C. New <sup>40</sup>K–<sup>40</sup>Ar dates for the Cretaceous–Quaternary magmatism of Northern Kamchatka (Russia). *C. R. Acad. Sci. Paris Serie II* **320**, 197–204 (1995).
- Park, J. *et al.* in *Plate Boundary Zones* (eds Stein, S. & Freymuller, J.) 295–324 (AGU, Geodynamics Series No. 30, American Geophysical Union, Washington DC, 2002).
- Kersting, A. B. & Arculus, R. J. Klyuchevskoy volcano, Kamchatka, Russia: The role of high-flux recharged, tapped, and fractionated magma chamber(s) in the genesis of high-Al<sub>2</sub>O<sub>3</sub> from high-MgO basalt. *J. Petrol.* **35**, 1–41 (1994).
- Davies, J. H. & von Blanckenburg, F. Slab breakoff: A model of lithosphere detachment and its test in the magmatism and deformation of collisional orogens. *Earth Planet. Sci. Lett.* **129**, 85–102 (1995).
- Wortel, M. J. R. & Spakman, W. Subduction and slab detachment in the Mediterranean-Carpathian region. *Science* **290**, 1910–1917 (2000).
- Lallemant, S. E., Font, Y., Bijwaard, H. & Kao, H. New insights on 3-D plates interaction near Taiwan from tomography and tectonic implications. *Tectonophysics* **335**, 229–253 (2001).
- Kosarev, G. L. *et al.* Seismic evidence for a detached Indian lithospheric mantle beneath Tibet. *Science* **283**, 1306–1309 (1999).
- Seber, D., Barazangi, M., Ibenbrahim, A. & Demnati, A. Geophysical evidence for lithospheric delamination beneath the Alboran Sea and Rif-Betic mountains. *Nature* **379**, 785–790 (1996).
- Gorbatov, A., Kostaglodov, V., Suarez, G. & Gordeev, E. Seismicity and structure of the Kamchatka subduction zone. *J. Geophys. Res.* **102**, 17883–17898 (1997).
- Fedorov, P. I. & Shapiro, M. N. Neogene volcanics of the Kamchatka isthmus and geodynamics of the Aleutian–Kamchatka junction. *Geotectonics* **32**, 122–137 (1998).
- Volynets, O. N. Geochemical types, petrology and genesis of late Cenozoic volcanic rocks from the Kurile–Kamchatka Island–Arc system. *Int. Geol. Rev.* **36**, 373–405 (1994).
- Boyd, T. M. & Creager, K. C. The geometry of Aleutian subduction: Three-dimensional seismic imaging. *J. Geophys. Res.* **96**, 2267–2291 (1991).
- Yogodzinski, G. M. *et al.* Geochemical evidence for the melting of subducting oceanic lithosphere at plate edges. *Nature* **409**, 500–504 (2001).
- Van der Hilst, R. D., Engdahl, E. R., Spakman, W. & Nolet, G. Tomographic imaging of subducted lithosphere below northwest Pacific island arcs. *Nature* **353**, 37–43 (1991).
- Gorbatov, A., Widiyantoro, A., Fukao, Y. & Gordeev, E. Signature of remnant slabs in the North Pacific from P-wave tomography. *Geophys. J. Int.* **142**, 27–36 (2000).
- Ritzwoller, M. H. & Levshin, A. L. Eurasian surface wave tomography: group velocities. *J. Geophys. Res.* **103**, 4839–4878 (1998).
- Ekstrom, G., Tromp, J. & Larson, E. W. F. Measurements and global models of surface waves propagation. *J. Geophys. Res.* **102**, 8137–8157 (1997).
- Trampert, J. & Woodhouse, J. H. Global phase velocity maps of Love and Rayleigh waves between 40 and 150 s period. *Geophys. J. Int.* **122**, 675–690 (1995).
- Ritzwoller, M. H., Shapiro, N. M., Barmin, M. P. & Levshin, A. L. Global surface wave diffraction tomography. *J. Geophys. Res.* (in the press).
- Shapiro, N. M. & Ritzwoller, M. H. Monte-Carlo inversion of broad-band surface wave dispersion for a global shear velocity model of the crust and upper mantle. *Geophys. J. Int.* (in the press).
- Levin, V. *et al.* Crust and upper mantle of Kamchatka from teleseismic receiver functions. *Tectonophysics* (in the press).
- Kepezhinskas, P. K. *et al.* Trace element and Sr–Nd–Pb isotopic constraints on a three-component model of Kamchatka Arc petrogenesis. *Geochim. Cosmochim. Acta* **61**, 577–600 (1997).
- Kepezhinskas, P. K., Defant, M. J. & Drummond, M. S. Progressive enrichment of island arc mantle by melt-peridotite interaction inferred from Kamchatka xenoliths. *Geochim. Cosmochim. Acta* **60**, 1217–1229 (1996).
- Braitseva, O. A., Melekestsev, I. V., Ponomareva, V. V. & Sulerzhitsky, L. D. Ages of calderas, large explosive craters and active volcanoes in the Kuril–Kamchatka region, Russia. *Bull. Volcanol.* **57**, 383–402 (1995).
- Ozerov, A. Y. The evolution of high-alumina basalts of the Klyuchevskoy volcano, Kamchatka, Russia, based on microprobe analysis of mineral inclusions. *J. Volcanol. Geotherm. Res.* **95**, 65–79 (2000).
- Turner, S., McDermott, F., Hawkesworth, C. & Kepezhinskas, P. A U-series study of lavas from Kamchatka and the Aleutians: Constraints on source composition and melting processes. *Contrib. Mineral. Petrol.* **133**, 217–234 (1998).
- Peyton, V. *et al.* Mantle flow at a slab edge: Seismic anisotropy in the Kamchatka region. *Geophys. Res. Lett.* **28**, 379–382 (2001).

## Acknowledgements

We acknowledge help with seismological fieldwork from the Kamchatka Experimental-Methodical Seismological Department of Russian Academy of Sciences and assistance

from IRIS Data Management Center in data and archive management. This work was funded by the National Science Foundation.

**Competing interests statement**

The authors declare that they have no competing financial interests.

Correspondence and requests for materials should be addressed to V.L. (e-mail: vadim.levin@yale.edu).

**A primitive fish close to the common ancestor of tetrapods and lungfish**

Min Zhu\* & Xiaobo Yu†

\* Institute of Vertebrate Paleontology and Paleoanthropology, Chinese Academy of Sciences, PO Box 643, Beijing 100044, China

† Department of Biological Sciences, Kean University, Union, New Jersey 07083, USA

The relationship of the three living groups of sarcopterygians or lobe-finned fish (tetrapods, lungfish and coelacanth) has been a matter of debate<sup>1–5</sup>. Although opinions still differ, most recent phylogenies suggest that tetrapods are more closely related to lungfish than to coelacanth<sup>6–10</sup>. However, no previously known fossil taxon exhibits a concrete character combination approximating the condition expected in the last common ancestor of tetrapods and lungfish—and it is still poorly understood how early sarcopterygians diverged into the tetrapod lineage (Tetrapodomorpha)<sup>7</sup> and the lungfish lineage (Dipnomorpha)<sup>7</sup>. Here we describe a fossil sarcopterygian fish, *Styloichthys changae* gen. et sp. nov., that possesses an eyestalk and which exhibits the character combination expected in a stem group close to the last common ancestor of tetrapods and lungfish. *Styloichthys* from the Lower Devonian of China bridges the morphological gap between stem-group sarcopterygians (*Psarolepis* and *Achoania*)<sup>10</sup> and basal tetrapodomorphs/basal dipnomorphs. It provides information that will help in the study of the relationship of early sarcopterygians, and which will also help to resolve the tetrapod–lungfish divergence into a documented sequence of character acquisition.

Sarcopterygii (Romer, 1955)  
*Styloichthys* gen. nov.

**Diagnosis.** A sarcopterygian characterized by relatively large pores (often spoon-shaped and arranged in parallel grooves) on the cosmine surface, a jagged margin between ethmosphenoid and otoccipital shields, an otoccipital with a wide flat ventral surface carrying no vestibular fontanelle, and a lower jaw with a ventrally protruding flange formed by prearticular and meckelian bone. *Styloichthys* differs from *Psarolepis* and *Achoania* in having a lyre-shaped trajectory of the supraorbital canal, a fenestra ventralis, small internasal cavities and three coronoids in the lower jaw. *Styloichthys* differs from tetrapodomorphs and dipnomorphs in having an eyestalk, a slender postorbital pila, and a cosmine surface with relatively large pores.

**Type species.** *Styloichthys changae* sp. nov.

**Etymology.** Generic name referring to the presence of postorbital pila (Greek *stylo*, pillar; *ichthys*, fish). Specific name in honour of M.-M. Chang for her contributions to palaeoichthyology.

**Holotype.** V8142.1, an anterior cranial portion, Institute of Vertebrate Paleontology and Paleoanthropology, Beijing.

**Age and locality.** Early Devonian (late Lochkovian), Xitun Formation, Qujing, East Yunnan, China.

**Remarks.** The new form (Figs 1 and 2) is represented by 20 anterior cranial portions (V8142.1–20), 7 posterior cranial portions (V8142.21–27), 18 lower jaws (V8143.1–18), one maxillary (V8143.19), 4 cheek bone plates (V8143.20–23), 5 cleithra (V8143.24–28) and 4 clavicles (V8143.29–32), all showing a unique cosmine surface with relatively large pores (though smaller than those in *Psarolepis* and *Achoania*<sup>10–12</sup>). The assignment of these specimens to the same form is further supported by matching morphology between the anterior and posterior cranial portions (Fig. 1a–f) and between the upper-jaw and lower-jaw structures (Figs 1c, i, and 2b, d).

**Description.** The most remarkable feature of *Styloichthys* is a recessed teardrop-shaped eyestalk area immediately behind the optic canal (Fig. 1e, g, h). This unfinished area has a well-defined natural margin as indicated by the surrounding periosteal lining which dips slightly into the unfinished recess, and corresponds to the eyestalk attachment area recently reported in basal bony fishes (*Psarolepis*, *Achoania* and *Ligulalepis* formerly known as AMF101607)<sup>10,13,14</sup>. Ventral to this eyestalk area, a cup-shaped depression serves for eye muscle attachment. *Styloichthys* also resembles *Psarolepis* and *Achoania* in having a postorbital pila (though splinter-like and much more slender) that forms a bridge between the top of the basiptyergoid process and the side of the braincase wall.

*Styloichthys* is quite close to *Youngolepis*<sup>15</sup> (a basal dipnomorph) in having an anteriorly positioned ethmoidal articulation, a fenestra ventralis and small internasal cavities, while other endocranial features seem intermediate between *Youngolepis* and *Psarolepis/Achoania*, such as a relatively broad suborbital ledge, a large notochordal pit, and a well-developed intracranial joint with a processus connectens giving a slightly convex profile to the posterior face of the ethmosphenoid (Fig. 1c, e, g, h). The well-ossified otoccipital (Fig. 1d, f) carries a large oval concave area for the basicranial muscle, a large keyhole-shaped bipartite facet for the hyomandibular and a large facet for the first infrapharyngealbranchial, but no vestibular fontanelle (also absent in some coelacanth and megalichthyid tetrapodomorphs such as *Cladrosymblema*<sup>16</sup>).

*Styloichthys* resembles *Youngolepis* and, to a lesser extent, *Powichthys*<sup>17</sup> (a basal dipnomorph) and *Kenichthys*<sup>18</sup> (a basal tetrapodomorph), in dermal bone features such as an inward and downward bending snout, a small independent premaxillary with high antero-medial portion and low postero-lateral portion (indicated by the outline of the premaxillary area and the sutural position of ethmoidal commissural canal), a large and long parasphenoid, a pineal foramen at the anterior margin of the parietals, a lyre-shaped trajectory of the supraorbital canal, groups of pores piercing the smooth surface between the relatively large cosmine pores, and a postparietal laterally flanked by more than two bones and posteriorly overlapped by the extrascapular. The compound cheek bone plate (corresponding to squamosal + quadratojugal + preopercular), maxillary, clavicle, and cleithrum with a tripartite scapulo-coracoid (Fig. 2) are also similar to those in *Youngolepis*<sup>19</sup>.

The lower jaw (Figs 1i, 2c, d) has three coronoids as indicated by three semilunar pockets along a shallow groove between the dentary and the prearticular, but is unique in having a very large adductor fossa (making up more than 50% of the lower jaw length), a convex ventral flange formed by prearticular and meckelian bone and protruding beyond the ventral border of infradentaries, and a prearticular carrying a shagreen of minute denticles dorsally and undulating parallel ridges ventrally.

To explore the phylogenetic position of *Styloichthys*, we modified the data matrix in ref. 10 by adding the *Styloichthys* codings and revising 21 codings for *Ligulalepis* and *Onychodus* based on newly available information<sup>13,20</sup>. Phylogenetic analysis<sup>21</sup> (see Supplementary Information) using the modified data matrix of 27 taxa and 158 characters yields 24 trees showing the same major groupings as ref. 10. *Styloichthys* is placed in a trichotomy with Dipnomorpha and